

Bulk-Boundary Correspondence in Non-Hermitian Systems

L. Jin^{1,*} and Z. Song¹

¹*School of Physics, Nankai University, Tianjin 300071, China*

Bulk-boundary correspondence is fundamental and important in topological physics; however, it is invalid in certain non-Hermitian systems. Here we report that the way of non-Hermiticity appearance may alter the system topology. The bulk-boundary correspondence is invalid if the introduced non-Hermiticity breaks the chiral-inversion symmetry of the Hermitian systems. After fixing the chiral-inversion symmetry by alternatively introducing the non-Hermiticity, the bulk-boundary correspondence recovers with all the bulk states being extended (the non-Hermitian skin effect vanishes). The vorticity of the topological defects in the vector field associated with the system Bloch Hamiltonian is a topological invariant, the change of which predicts the topological phase transition and the (non)existence of edge states. Our findings provide insightful understanding for the topological features and the bulk-boundary correspondence in non-Hermitian systems.

Introduction.—Topological theory has been well established in condensed matter physics for Hermitian systems [1–27]. In parallel, non-Hermitian physics exhibits considerable intriguing features [28–47]; the exceptional point (EP), which has no Hermitian correspondence, exhibits different topology as Hermitian degeneracy point [48–64]. Recently, the experimental realization of topological systems in optical lattice boosts the development of topological photonics [65–71]; the unexpected novel interface states appear between non-Hermitian periodic media with distinct topologies [72–84]. These progresses stimulate the investigations of non-Hermitian topological systems [85–109]. The non-Hermitian band theory and topological characterization are developed [89–93], the Chern number, the generalized Berry phase and winding numbers employed the left and right eigenstates [30, 34] are quantized as topological invariants [89–91].

The existence of gapless edge states of a system under open boundary condition (OBC) is predictable from the change of topological invariants associated with the bulk topology of system under periodical boundary condition (PBC), known as the (conventional) bulk-boundary correspondence, which is ubiquitously applicable in Hermitian systems. However, the breakdown of bulk-boundary correspondence exists in non-Hermitian systems; and the systems under PBC and OBC have dramatically different energy spectra [83, 98, 99, 107]. To deal with this problem, the biorthogonal bulk-boundary correspondence uses a coined biorthogonal polarization to distinguish different topological phases, and the edge states in the system under OBC [92]; alternatively, the non-Bloch bulk-boundary correspondence has been established. A non-Bloch topological invariant defined in a deformed Brillouin zone can predict the topological phase transition (TPT) and the non(existence) of edge states [93].

In contrast, the non-Hermiticity does not inevitably destroy the bulk-boundary correspondence [73, 74], and its validity is verified in a \mathcal{PT} -symmetric non-Hermitian extension of Su-Schrieffer-Heeger (SSH) model [110] with staggered couplings and losses [76, 78, 81, 84]. The existence of topologically protected states at the interface

of media with distinct topologies are predicted from the bulk topology, characterized by a Zak phase related winding number [84].

In this Letter, we report that *non-Hermiticity may alter the system topology and symmetry plays an important role* for the validity of bulk-boundary correspondence in non-Hermitian systems. We elucidate that the breakdown of bulk-boundary correspondence in the non-Hermitian systems [83, 92, 93, 98, 99] attributes to the absence of chiral-inversion symmetry protection when non-Hermiticity is introduced, which directly induces a TPT. After fixing the chiral-inversion symmetry through alternatively introducing the non-Hermiticity, the energy spectrum under OBC is not altered; remarkably, the bulk-boundary correspondence is valid and the bulk topology of the Bloch Hamiltonian for the system under PBC correctly predicts the (non)existence of topological edge states for the system under OBC. The gapless degeneracy points as TPT points correspond to the topological defects with vortex and antivortex in a vector field that associated with the Bloch Hamiltonian; and the vorticity of the topological defects is a topological invariant.

Non-Hermitian SSH model.—We consider the Bloch Hamiltonians of non-Hermitian systems

$$H(k) = \vec{B} \cdot \vec{\sigma}, \quad (1)$$

where $\vec{B} = (B_x, B_y, B_z)$ is the effective complex magnetic field and $\vec{\sigma}$ is a vector of Pauli matrices $\vec{\sigma} = (\sigma_x, \sigma_y, \sigma_z)$. For a dimerized one-dimensional (1D) lattice system a [Fig. 1(a)] described by a non-Hermitian SSH model, the asymmetric intracell coupling strength ($|\mu| \neq |\nu|$) raises the non-Hermiticity. The intercell coupling is denoted as t_2 , which is considered symmetric for simplicity [111]. Under PBC, the topological system is translational symmetric, the Bloch Hamiltonian in the k -space is

$$H_a(k) = \begin{pmatrix} 0 & \mu + t_2 e^{-ik} \\ \nu + t_2 e^{ik} & 0 \end{pmatrix}. \quad (2)$$

The eigenvalues $E_{a,\pm} = \pm \sqrt{t_2^2 + \mu\nu + t_2(\mu e^{ik} + \nu e^{-ik})}$ are symmetric [Fig. 2(a)]. For the discrete lattice size

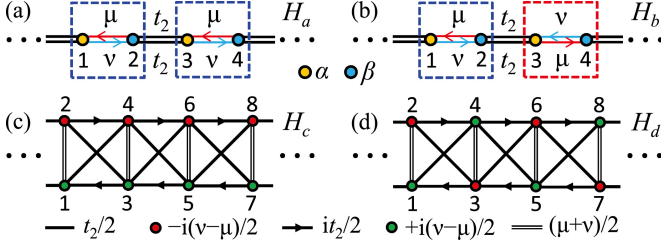


FIG. 1. (a, b) Schematic of the 1D SSH lattices, the unit cells are indicated in the rectangles. (c) and (d) are the equivalent quasi-1D square lattices of (a) and (b), respectively [112]. $H_\rho(k)$ (H_ρ) is the Hamiltonian ρ in the k -space (real-space), where $\rho = a, b, c, d$. The system sizes are all $N = 4n$.

$N = 4n$, the wave vector is $k = \pi m/n$, $m \in [1, 2n]$ (m, n are positive integers).

To analysis the topological features of the non-Hermitian system a , we set

$$\mu = t_1 - \gamma, \nu = t_1 + \gamma, \quad (3)$$

and consider that t_1, t_2, γ are real numbers. System a has the chiral symmetry $\mathcal{S}H_a(k)\mathcal{S}^{-1} = -H_a(k)$, the time-reversal symmetry $\mathcal{T}H_a(k)\mathcal{T}^{-1} = H_a(-k)$, and the charge-conjugation (particle-hole) symmetry $(\mathcal{S}\mathcal{T})H_a(k)(\mathcal{S}\mathcal{T})^{-1} = -H_a(-k)$ [112]; its Hamiltonian in the real-space fulfills the constrains $U_S H_a U_S^{-1} = -H_a$, $U_{\mathcal{T}} H_a^* U_{\mathcal{T}}^{-1} = H_a$, and $U_{\mathcal{S}\mathcal{T}} H_a^* U_{\mathcal{S}\mathcal{T}}^{-1} = -H_a$, respectively [9, 10, 25], where $*$ is the complex conjugation. For complex γ , only the chiral symmetry holds, the time-reversal symmetry and the charge-conjugation symmetry vanish.

For a Hamiltonian H in the real-space and its Bloch Hamiltonian $H(k)$ in the k -space, H is denoted as chiral-inversion symmetric under the constrains

$$(\mathcal{S}\mathcal{P})H(k)(\mathcal{S}\mathcal{P})^{-1} = -H(-k), U_{\mathcal{S}\mathcal{P}} H U_{\mathcal{S}\mathcal{P}}^{-1} = -H. \quad (4)$$

$\mathcal{S}\mathcal{P}$ and all the operators U with a subscript are unitary. Notably, the constrains are for a *combined chiral-inversion symmetry*, while the individual chiral and inversion are not necessarily holds separately.

In Hermitian case ($\gamma = 0$), system a is chiral-inversion symmetric; two isolated gapless degeneracy points exist under PBC [Fig 2(d)], and the eigenstates are symmetric or antisymmetric. However, if asymmetric coupling is introduced, the spectra and the gap closing points under PBC [Fig 2(a)] and OBC [Fig 2(c)] are dramatically different [92, 93, 99, 107], and the bulk-boundary correspondence is invalid; instead, the biorthogonal bulk-boundary correspondence and non-Bloch bulk-boundary correspondence are suggested [92, 93]. Notably, unlike the alternative gain and loss [76, 78, 81, 84], the asymmetric coupling breaks the chiral-inversion symmetry, two gapless degeneracy points split into two pairs of isolated gapless EPs [Figs. 2(a) and 2(d)] [46], which induces a TPT [113]. The eigenstates under OBC are no longer symmetric or

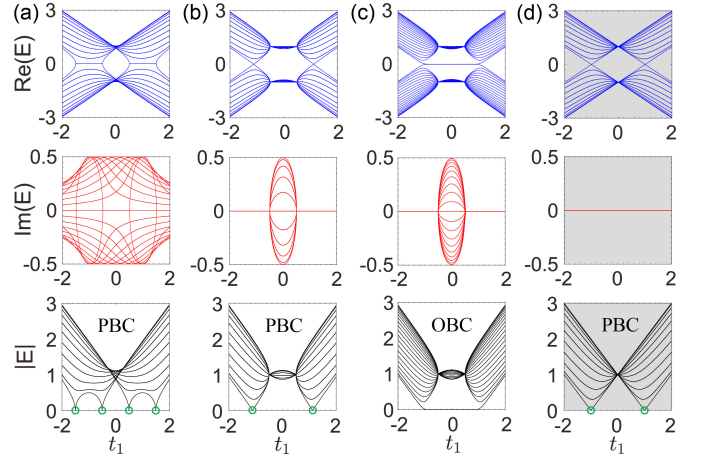


FIG. 2. Energy spectra for (a-c) non-Hermitian systems and (d) Hermitian SSH model. (a) [(b)] for systems in Figs. 1(a) and 1(c) [Figs. 1(b) and 1(d)] under PBC. (c) Energy spectra under OBC with one intercell coupling t_2 missing for all the systems in Figs. 1(a)–1(d). The gapless points are marked inside the green circles. The system parameters are $\gamma = 1/2$ in (a-c) and $\gamma = 0$ in (d), $t_2 = 1$, and $N = 40$.

antisymmetric without the symmetry protection; and all the eigenstates are localized at the system boundary (the non-Hermitian skin effect) [92, 93, 98].

Bulk-Boundary Correspondence.—Non-Hermiticity is alternatively introduced in system b [Fig. 1(b)], where the chiral-inversion symmetry holds. Under the symmetry protection, two degeneracy points can move without splitting into EP pairs [Figs. 2(b) and 2(d)]; the bulk-boundary correspondence recovers in both the region with entirely real spectra and the region with complex spectra [Figs. 2(b) and 2(c)].

Systems a and b have different unit cells; however, they possess identical energy spectra under OBC [Fig. 2(c)], but with significantly different eigenstates: All the bulk states in system b are extended, and only the edge states are localized [Figs. 4(c)–4(e)]; the non-Hermitian skin effect vanishes. These reflect the distinct topologies of systems a and b , and manifest a fact that *the way of non-Hermiticity appearance affects the system topology*.

The recovery of bulk-boundary correspondence enables predicting the existence of topological protected edge states from the bulk topology of system b . The Bloch Hamiltonian of system b has a four-site unit cell

$$H_b(k) = \begin{pmatrix} 0 & \mu & 0 & t_2 e^{-ik} \\ \nu & 0 & t_2 & 0 \\ 0 & t_2 & 0 & \nu \\ t_2 e^{ik} & 0 & \mu & 0 \end{pmatrix}. \quad (5)$$

System b has the chiral symmetry, the inversion symmetry, and the chiral-inversion symmetry [112]. The eigenvalues $E_{b,\pm,\pm} = \pm\sqrt{t_2^2 + \mu\nu} \pm 2t_2\sqrt{\mu\nu}\cos(k/2)$ ($k = 2\pi m/n$, $m \in [1, n]$) are symmetric. Through a unitary

transformation $U_{\mu\nu} = \text{diag}(\sqrt{\nu}, \sqrt{\mu}, \sqrt{\mu}, \sqrt{\nu})$ with only nonzero diagonal elements, we obtain an equivalent Bloch Hamiltonian $U_{\mu\nu} H_b(k) U_{\mu\nu}^{-1}$, which is system *a* with all the asymmetric couplings substituted by the symmetric couplings $\sqrt{\mu\nu}$ and taken two unit cells as a compound one [112]. This equivalent system has a two-site unit cell and the Bloch Hamiltonian is

$$h_b(k) = \begin{pmatrix} 0 & \sqrt{\mu\nu} + t_2 e^{-ik} \\ \sqrt{\mu\nu} + t_2 e^{ik} & 0 \end{pmatrix}. \quad (6)$$

$E_{b,\pm} = \pm\sqrt{t_2^2 + \mu\nu + 2t_2\sqrt{\mu\nu}\cos(k)}$ are the eigenvalues of $h_b(k)$, ($k = \pi m/n$, $m \in [1, 2n]$). System *b* and system *a* with symmetric coupling $\sqrt{\mu\nu}$ are topological equivalent, and the topological features are reflected from the bulk topology of $h_b(k)$. Notably, $h_b(k)$ is identical with that found in Ref. [93] through solving H_a under OBC.

Topological invariant.—Recently, the topology invariants are established in the non-Hermitian systems [89–91, 93, 97, 102]. These are usually done by using the biorthonormal eigenstates (left and right eigenstates) of the system Bloch Hamiltonian. The Chern number defined via Berry curvature [90, 91, 102] and the generalized Berry phase defined via the argument of the effective magnetic field [89, 90, 97] are quantized.

We alternatively use the vorticity of the topological defects in a vector field that associated with the Bloch Hamiltonian to characterize the system topology [113–115]. Notice that $h_b(k) = (\sqrt{\mu\nu} + t_2 \cos k) \sigma_x + (t_2 \sin k) \sigma_y$, a two-component vector field $\mathbf{F}(\mathbf{k}) = (\langle \sigma_x \rangle, \langle \sigma_y \rangle)$ is defined from the average values of the Pauli matrices under the eigenstates of $h_b(k)$. The topological defects in the vector field associated with vortices (red dots) and antivortices (blue dots) are the TPT points. The winding number $w = \oint_L (2\pi)^{-1} (\hat{F}_x \nabla \hat{F}_y - \hat{F}_y \nabla \hat{F}_x) d\mathbf{k}$ is a topological invariant characterizing the vorticity of the TPT points and $2\pi w$ accounts the varying direction of $\mathbf{F}(\mathbf{k})$ in the closed loop L in the parameter plane $\mathbf{k} = (k, t_2)$, where $\hat{F}_{x(y)} = F_{x(y)} / \sqrt{F_x^2 + F_y^2}$, $\nabla = \partial/\partial\mathbf{k}$. $\mathbf{F}(\mathbf{k})$ is depicted in Figs. 3(a) and 3(b); the topological properties revealed from the vector field defined in the parameter plane are in accord with that defined in the Brillouin zone of a two-dimensional (2D) brick wall lattice in the momentum space $\mathbf{k} = (k_x, k_y)$; along one direction of the 2D lattice is the 1D system *b* [112]. The varying direction of the vector field $\mathbf{F}(\mathbf{k})$ accumulated in the loop L is $\pm 2\pi$ ($\pm\pi$) in Fig. 3(a) [Fig. 3(b)] if L encircling a TPT point, the plus (minus) sign corresponds to the vortex (antivortex); otherwise, if L does not encircle a TPT point, the varying direction is zero. The phase diagram is plotted in Fig. 3(c). For $\mu\nu > 0$, the TPT occurs at $t_2^2 - \mu\nu = 0$; as the non-Hermiticity increases, the band gap in the region with complex spectrum inside the two high order EPs diminishes and closes at $t_1 = 0$ when $\gamma^2 = t_2^2$ [116]. The high order EP [30, 47]

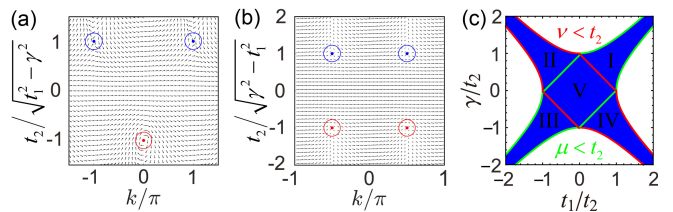


FIG. 3. The vector field $\mathbf{F}(\mathbf{k})$ associated with $E_{b,+}$ of $h_b(k)$ for (a) $\mu\nu = t_1^2 - \gamma^2 > 0$ and (b) $\mu\nu = t_1^2 - \gamma^2 < 0$. The red (blue) circles indicate the TPT points with vortices (antivortices), which appear at $(k, t_2) = (0, -\sqrt{t_1^2 - \gamma^2})$ or $(\pm\pi, \sqrt{t_1^2 - \gamma^2})$ in (a) and at $(k, t_2) = (\pm\pi/2, \pm\sqrt{\gamma^2 - t_1^2})$ in (b). (c) Phase diagram, two topological zero edge states exist in the area $-t_2^2 < \mu\nu < t_2^2$ in blue for one intercell coupling t_2 missing. The green (red) ribbon indicates $\mu < t_2$ ($\nu < t_2$) with the edge states localized on the right (left) boundary.

occurs at $\mu\nu = 0$ ($t_1 = \pm\gamma$) [Fig. 2(b)]; where half of the eigenstates are two-state coalesced at energy t_2 and $-t_2$, respectively. For $\mu\nu < 0$, $t_2^2 + \mu\nu = 0$ yields another boundary for the zero edge state. The TPT points are at

$$\pm(t_1^2 - \gamma^2) = t_2^2, \quad (7)$$

being coincident with those obtained in alternative manners [92, 93]. Notably, the gapless points are degeneracy points (EPs) at $t_1^2 = +(-)t_2^2 + \gamma^2$ and are topological defects carrying integer (half-integer) vortices or antivortices. Two topological zero edge states exist in between regions $\gamma^2 - t_2^2 < t_1^2 < \gamma^2 + t_2^2$ for one intercell coupling t_2 vanishing under OBC [120]. As γ increases, the region with edge states expands when $\gamma^2 \leq t_2^2$, but shrinks when $\gamma^2 > t_2^2$.

Topological edge states.—The bulk topology relates to the (dis)appearance of edge states at the interfaces where topological invariant changes. We consider all the unit cells being complete ($N = 4n$) with one intercell coupling t_2 vanishing (the Supplemental Material provides the cases of defective unit cell at boundary [112]). In system *b*, two edge states localize on the left and right boundaries, respectively in all blue regions of Fig. 3(c). In system *a*, the left and right edge states localize on the left and right boundaries, respectively only in region V, both two edge states localize on the right (left) boundary in regions I and III (II and IV). Figures 4(a) and 4(b) show the edge states of systems *a* and *b* under OBC.

For system *b*, the edge state localized on the left boundary of the system is $\psi_{2j} = 0$ and

$$\psi_{2j+1} = -[(\mu + \nu) + (-1)^j(\mu - \nu)] / (2t_2) \psi_{2j-1}, \quad (8)$$

at large system size limit ($N \gg 1$). Correspondingly, the other edge state localized on the right boundary of the system is a left-right spatial reflection of the left edge state. Anomalous edge states localized at single unit cell at boundary are found at the high order EPs ($t_1^2 = \gamma^2$) [83, 89]. At $t_1 = -\gamma$, the left edge state is $\psi_1 = 1$ and

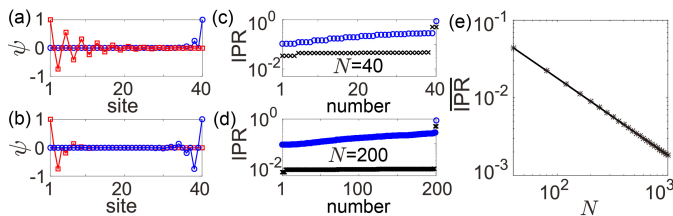


FIG. 4. (a), (b) Zero edge states for systems a and b ($N = 40$) under OBC, respectively. (c, d) The IPR of all the eigenstates, the blue circles (black crosses) are for system a (b). (e) The averaged IPR for all the bulk states of system b (scales as $1/N$). The system parameters are $t_1 = 1/4$, $\gamma = 1/2$, and $t_2 = 1$; notably, the bulk states are mostly complex [Fig. 2(c)].

the right edge state is $\psi_N = 1$; at $t_1 = \gamma$, the left edge state is $\psi_1 = -(+)\psi_3 = 1$ and the right edge state is $\psi_N = -(+)\psi_{N-2} = 1$ when $t_1/t_2 > 0$ ($t_1/t_2 < 0$).

In contrast, for system a , the edge state localized on the left boundary is $\psi_{2j} = 0$ and $\psi_{2j+1} = (-v/t_2)\psi_{2j-1}$; the edge state localized on the right boundary has different decay rate $-\mu/t_2$: The edge state is $\psi_{2j-1} = 0$ and $\psi_{N-2j} = (-\mu/t_2)\psi_{N+2-2j}$ [92, 93]. If $|\nu/t_2| > 1$ ($|\mu/t_2| > 1$) as indicated in Fig. 3(c) by the red lines (green lines), both edge states localize on the right (left) boundary. The edge states are $\psi_1 = 1$ ($\psi_N = 1$) for $t_1/t_2 < 0$ ($t_1/t_2 > 0$) at the high order EPs.

In Figs. 4(c) and 4(d), we depict the inverse participation ratio (IPR) $\sum_j |\psi_j|^4$ for all the eigenstates (normalized to unity, $\sum_j |\psi_j|^2 = 1$). As the system size increases, the IPR for the eigenstates of system a is system size insensitive; thus, all the eigenstates are localized (non-Hermitian skin effect [92, 93]); the IPR for the bulk eigenstates of system b is inversely proportional to the system size [Fig. 4(e)], which indicates that all the bulk states are extended.

Discussion.—The quasi-1D systems c and d [Figs. 1(c) and 1(d)] are equivalent systems of the 1D systems a and b [Figs. 1(a) and 1(b)], respectively. 1D and quasi-1D systems are connected through a unitary transformation and have identical energy spectra [112]. The chiral symmetry, the charge-conjugation symmetry [82, 100, 117–119], and the \mathcal{PT} -symmetry [47] in systems c and d ensure that the eigenvalues appear in pairs of $(E, -E)$, $(E, -E^*)$, and (E, E^*) , respectively; thus, $(E, -E, E^*, -E^*)$ appear in pairs. The bulk-boundary correspondence is invalid in system c without chiral-inversion symmetry [83, 94, 98], but is valid in system d with chiral-inversion symmetry; the ways of the gain and loss appearance affect the system topology.

The chiral-inversion symmetry holds and the bulk-boundary correspondence is valid for complex μ and ν . For $\gamma = |r|e^{i\theta}$ ($-\pi \leq \theta \leq \pi$), the TPT occurs at

$$(t_1^2 - |r|^2)^2 + 4t_1^2|r|^2 \sin^2 \theta = t_2^4, \quad (9)$$

and $\cos^2(k) = [t_2^2 + t_1^2 - |r|^2 \cos(2\theta)] / (2t_2^2)$ are the gapless

degeneracy points. These can be directly obtained from the gap closing points in the spectrum of $h_b(k)$ ($E_{b,\pm}$). Equation (7) is a special case of real μ and ν at $\theta = 0$.

The non-Hermitian asymmetric coupling can be realized through introducing a synthetic imaginary gauge field [121, 122]; in an array of coupled resonators that consists of primary resonators that evanescently coupled with the assistant of auxiliary resonators, the auxiliary resonators have half perimeter gain and half perimeter loss, leading to the amplification and attenuation for the coupling amplitudes in opposite tunneling directions. Alternatively, the asymmetric coupling can be realized via synthetic real gauge field and a pair of gain and loss [123]; the symmetric and anti-symmetric supermodes enable an asymmetric coupling between them. Implementation of asymmetric coupling strength with ultracold atoms in optical lattice is possible [99].

Considering a minus sign in front of the asymmetric coupling in the red unit cell in Fig. 1(b), we denote the system as b' , which relates to system b through a unitary transformation; system b' has the chiral symmetry, but the inversion symmetry is violated. If the gain and loss terms $\{i\Gamma, -i\Gamma, i\Gamma, -i\Gamma\}$ are nonzero in system b as in Refs. [78, 81, 84], both the chiral symmetry and the inversion symmetry are violated; under OBC, this system and system a with $\{i\Gamma, -i\Gamma\}$ in the unit cell possess identical spectra. If $i\Gamma$ is alternatively introduced in form of $\{i\Gamma, -i\Gamma, -i\Gamma, i\Gamma\}$, the chiral symmetry is violated, but the inversion symmetry holds [112]. The chiral-inversion symmetry holds in all three cases. The gapless degeneracy (exceptional) points protected by the chiral-inversion symmetry in systems under PBC and OBC are in accord with each other. Notice that the introduced non-Hermiticity does not break the chiral-inversion symmetry of systems investigated in Refs. [73, 74, 76, 78, 81, 84, 102], where the bulk-boundary correspondence is applicable.

Conclusion.—The non-Hermiticity alters the system topology by breaking the chiral-inversion symmetry of the Hermitian system, and leads to the breakdown of (conventional) bulk-boundary correspondence. When the combined chiral-inversion symmetry is recovered via alternatively introducing the non-Hermiticity, the bulk-boundary correspondence recurs. The chiral-inversion symmetry protects the TPT points, which are the topological defects with vortex and antivortex in the vector field that associated with the Bloch Hamiltonian and correspond to the gapless degeneracy points in the energy spectrum. The vorticity of the TPT points is a topological invariant, which characterizes the bulk topology of the system and its changes correctly predict the (non)existence of topological boundary states in the non-Hermitian systems.

We acknowledge the support of NSFC (Grant Nos. 11605094 and 11874225).

SUPPLEMENTAL MATERIAL

Equivalence between systems and their connections

The systems discussed have the total lattice size $N = 4n$, the labels are marked in Fig. 1. In the real-space, through a unitary transformation

$$U = I_{2n} \otimes (i\sigma_x + I_2), \quad (10)$$

the systems a and b change into their corresponding quasi-1D systems c and d , respectively; i.e., $H_{c(d)} = UH_{a(b)}U^{-1}$; where \otimes is the Kronecker product and I_{2n} is the $2n \times 2n$ identical matrix.

In the k -space, the Bloch Hamiltonians are

$$H_a(k) = \begin{pmatrix} 0 & \mu + t_2 e^{-ik} \\ \nu + t_2 e^{ik} & 0 \end{pmatrix}, H_c(k) = \frac{1}{2} \begin{pmatrix} i\nu - i\mu - 2t_2 \sin k & \mu + \nu + 2t_2 \cos k \\ \mu + \nu + 2t_2 \cos k & i\mu - i\nu + 2t_2 \sin k \end{pmatrix}, \quad (11)$$

$$H_b(k) = \begin{pmatrix} 0 & \mu & 0 & t_2 e^{-ik} \\ \nu & 0 & t_2 & 0 \\ 0 & t_2 & 0 & \nu \\ t_2 e^{ik} & 0 & \mu & 0 \end{pmatrix}, H_d(k) = \frac{1}{2} \begin{pmatrix} i\nu - i\mu & \mu + \nu & it_2(1 - e^{-ik}) & t_2(1 + e^{-ik}) \\ \mu + \nu & i\mu - i\nu & t_2(1 + e^{-ik}) & -it_2(1 - e^{-ik}) \\ -it_2(1 - e^{ik}) & t_2(1 + e^{ik}) & i\mu - i\nu & \mu + \nu \\ t_2(1 + e^{ik}) & it_2(1 - e^{ik}) & \mu + \nu & i\nu - i\mu \end{pmatrix}. \quad (12)$$

The Bloch Hamiltonians $H_a(k)$ and $H_c(k)$ are connected via $U_{ac} = (i\sigma_x + I_2)$ as

$$U_{ac}H_a(k)U_{ac}^{-1} = H_c(k), \quad (13)$$

the Bloch Hamiltonians $H_b(k)$ and $H_d(k)$ are connected via $U_{bd} = I_2 \otimes (i\sigma_x + I_2)$ as

$$U_{bd}H_b(k)U_{bd}^{-1} = H_d(k). \quad (14)$$

For the sake of comparison, the Bloch Hamiltonians of systems a and c are alternatively shown in form of

$$H'_a(k) = \begin{pmatrix} 0 & \mu & 0 & t_2 e^{-ik} \\ \nu & 0 & t_2 & 0 \\ 0 & t_2 & 0 & \mu \\ t_2 e^{ik} & 0 & \nu & 0 \end{pmatrix}, H'_c(k) = \frac{1}{2} \begin{pmatrix} i\nu - i\mu & \mu + \nu & it_2(1 - e^{-ik}) & t_2(1 + e^{-ik}) \\ \mu + \nu & i\mu - i\nu & t_2(1 + e^{-ik}) & -it_2(1 - e^{-ik}) \\ -it_2(1 - e^{ik}) & t_2(1 + e^{ik}) & i\nu - i\mu & \mu + \nu \\ t_2(1 + e^{ik}) & it_2(1 - e^{ik}) & \mu + \nu & i\mu - i\nu \end{pmatrix}. \quad (15)$$

where two unit cells are considered as a compound one, $U_{bd}H'_a(k)U_{bd}^{-1} = H'_c(k)$. In the discrete systems with lattice size $N = 4n$, the wave vector k is $k = \pi m/n$, $m \in [1, 2n]$ (m, n are positive integers) for the Bloch Hamiltonians $H_a(k)$ and $H_c(k)$ with a two-site unit cell, and the wave vector k is $k = 2\pi m/n$, $m \in [1, n]$ for the Bloch Hamiltonians $H'_a(k)$, $H_b(k)$, $H'_c(k)$, and $H_d(k)$ with a four-site unit cell. Notably, $H_a(k)$ and $H'_a(k)$ [$H_c(k)$ and $H'_c(k)$] yield identical energy bands.

Symmetries

Chiral symmetry.—The systems discussed in Fig. 1 have chiral symmetry. A linear operator U_S defines the chiral symmetry in the real-space. For systems a and b , the chiral operator \mathcal{S} indicates that the opposite signs are implemented on the two sublattices indicated by different colors $U_S = I_{2n} \otimes \sigma_z$; for systems c and d , the chiral operator \mathcal{S} is $U_S = I_{2n} \otimes \sigma_y$; acting \mathcal{S} on the Hamiltonians result in

$$U_S H_\rho U_S^{-1} = -H_\rho, \quad (16)$$

where $\rho = a, b, c, d$. For the Bloch Hamiltonians $H_\rho(k)$ in the k -space, they hold the chiral symmetry because

$$\mathcal{S} H_\rho(k) \mathcal{S}^{-1} = -H_\rho(k), \quad (17)$$

where $\mathcal{S} = \sigma_z$ for system a [$\mathcal{S} = I_2 \otimes \sigma_z$ for the $H'_a(k)$], $\mathcal{S} = \sigma_y$ for system c [$\mathcal{S} = I_2 \otimes \sigma_y$ for the $H'_c(k)$], $\mathcal{S} = I_2 \otimes \sigma_z$ for system b , and $\mathcal{S} = I_2 \otimes \sigma_y$ for system d .

Time-reversal symmetry.—In case that the non-Hermitian asymmetric couplings μ and ν are real, the time-reversal symmetry holds

$$U_{\mathcal{T}} H_{\rho}^* U_{\mathcal{T}}^{-1} = H_{\rho}, \quad (18)$$

where $\rho = a, b, c, d$. $U_{\mathcal{T}}$ is the identical matrix I_{4n} for systems a and b ; and $U_{\mathcal{T}}$ is the spatial reflection in either the horizontal or the vertical direction for systems c and d as shown in Fig. 1. In the k -space,

$$\mathcal{T} H_{\rho}(k) \mathcal{T}^{-1} = H_{\rho}(-k), \quad (19)$$

$\mathcal{T} = I_2 K$ for system a [$\mathcal{T} = I_4 K$ for the $H'_a(k)$] and $\mathcal{T} = I_4 K$ for system b , where K is the complex conjugation. $\mathcal{T} = \sigma_x K$ for system c [$\mathcal{T} = (I_2 \otimes \sigma_x) K$ for the $H'_c(k)$] and $\mathcal{T} = (I_2 \otimes \sigma_x) K$ for system d .

Charge-conjugation (particle-hole) symmetry.—The combination of \mathcal{ST} yields the charge-conjugation (\mathcal{C}) [25, 82, 100, 118, 119], the charge-conjugation symmetric system satisfies

$$U_{\mathcal{C}} H_{\rho}^* U_{\mathcal{C}}^{-1} = -H_{\rho}, \quad (20)$$

$$\mathcal{C} H_{\rho}(k) \mathcal{C}^{-1} = -H_{\rho}(-k). \quad (21)$$

The charge-conjugation symmetry is also called the particle-hole symmetry. For systems $\rho = a, b, c, d$ under periodical boundary condition (PBC), the unitary transformation is

$$U_{\mathcal{C}} = I_{2n} \otimes \sigma_z. \quad (22)$$

In the k -space, we have

$$(\sigma_z K) H_{a,c}(k) (\sigma_z K)^{-1} = -H_{a,c}(-k), \quad (23)$$

for $H_a(k)$ and $H_c(k)$, and

$$[(I_2 \otimes \sigma_z) K] H_{b,d}(k) [(I_2 \otimes \sigma_z) K]^{-1} = -H_{b,d}(-k). \quad (24)$$

for $H_b(k)$ and $H_d(k)$ [$\mathcal{C} = (I_2 \otimes \sigma_z) K$ also for $H'_a(k)$ and $H'_c(k)$]. Notably, both the time-reversal symmetry and the charge-conjugation symmetry vanish when μ and ν are complex.

Chiral-inversion symmetry.—The introduced non-Hermiticity breaks the chiral-inversion symmetry of systems a and c . In contrast, through alternatively introducing the non-Hermiticity, systems b and d possess the chiral-inversion symmetry. In the real-space, the Hamiltonians of systems b and d satisfy

$$(P_{2n} \otimes \sigma_y) H_b (P_{2n} \otimes \sigma_y)^{-1} = -H_b, \quad (25)$$

$$(P_{2n} \otimes \sigma_z) H_d (P_{2n} \otimes \sigma_z)^{-1} = -H_d. \quad (26)$$

where P_{2n} is a 90 degrees rotation of I_{2n} . In the k -space, the Bloch Hamiltonians of systems b and d satisfy

$$(\sigma_x \otimes \sigma_y) H_b(k) (\sigma_x \otimes \sigma_y)^{-1} = -H_b(-k), \quad (27)$$

$$(\sigma_x \otimes \sigma_z) H_d(k) (\sigma_x \otimes \sigma_z)^{-1} = -H_d(-k). \quad (28)$$

Topological characterization

We intend to obtain the bulk topological properties and the topological invariant of system b . Notice that the Bloch Hamiltonian of system b is a 4×4 matrix; however, we will show that $H_b(k)$ possesses identical topological features as $H_a(k) = \vec{B} \cdot \vec{\sigma}$ with symmetric coupling, the topological characterizations of which are well established. In the following, we first show the topological equivalent system of system b , and then calculate the vector field associated with the Bloch Hamiltonian of the equivalent system; the vortices and antivortices in the vector field indicate the topological phase transition points and reflect the topological properties of system b .

To elucidate the topologically equivalent system, we consider that t_1 and γ are real positive numbers in form of $\mu = t_1 - \gamma$ and $\nu = t_1 + \gamma$ as listed in Eq. (3); discussions on other cases are similar following the same procedure below. $\mu\nu = 0$ corresponds to the high order exceptional points.

For $\mu\nu > 0$, μ , ν and $\sqrt{\mu\nu}$ are positive real numbers. The Bloch Hamiltonian $H_b(k)$ under a unitary transformation

$$U_{\mu\nu>0} = \begin{pmatrix} \sqrt{\nu} & 0 & 0 & 0 \\ 0 & \sqrt{\mu} & 0 & 0 \\ 0 & 0 & \sqrt{\mu} & 0 \\ 0 & 0 & 0 & \sqrt{\nu} \end{pmatrix}, \quad (29)$$

yields

$$U_{\mu\nu>0} H_b(k) U_{\mu\nu>0}^{-1} = \begin{pmatrix} 0 & \sqrt{\mu\nu} & 0 & t_2 e^{-ik} \\ \sqrt{\mu\nu} & 0 & t_2 & 0 \\ 0 & t_2 & 0 & \sqrt{\mu\nu} \\ t_2 e^{ik} & 0 & \sqrt{\mu\nu} & 0 \end{pmatrix}, \quad (30)$$

which equals to the Bloch Hamiltonian of system a with two unit cells as a compound unit cell after replacing all the asymmetric couplings μ and ν with the symmetric coupling $\sqrt{\mu\nu}$; otherwise, for $\mu\nu < 0$, the numbers $-\mu$, ν and $\sqrt{-\mu\nu}$ are positive real numbers. The Bloch Hamiltonian $H_b(k)$ under a unitary transformation

$$U_{\mu\nu<0} = \begin{pmatrix} \sqrt{\nu} & 0 & 0 & 0 \\ 0 & i\sqrt{-\mu} & 0 & 0 \\ 0 & 0 & i\sqrt{-\mu} & 0 \\ 0 & 0 & 0 & \sqrt{\nu} \end{pmatrix}, \quad (31)$$

yields

$$U_{\mu\nu<0} H_b(k) U_{\mu\nu<0}^{-1} = \begin{pmatrix} 0 & i\sqrt{-\mu\nu} & 0 & t_2 e^{-ik} \\ i\sqrt{-\mu\nu} & 0 & t_2 & 0 \\ 0 & t_2 & 0 & i\sqrt{-\mu\nu} \\ t_2 e^{ik} & 0 & i\sqrt{-\mu\nu} & 0 \end{pmatrix}, \quad (32)$$

which is the Bloch Hamiltonian of system a with two unit cells as a compound unit cell after replacing all the asymmetric couplings μ and ν with the symmetric coupling $i\sqrt{-\mu\nu}$.

Therefore, the bulk topology of system b is characterized by the Bloch Hamiltonian of $H_a(k)$ with the symmetric couplings. The equivalent system is Hermitian when $\mu\nu > 0$, but is non-Hermitian when $\mu\nu < 0$; both cases hold the chiral-inversion symmetry.

For $\mu\nu > 0$, the Bloch Hamiltonian of Eq. (30) is rewritten with a two-site unit cell in the form of

$$h_b(k) = \begin{pmatrix} 0 & \sqrt{\mu\nu} + t_2 e^{-ik} \\ \sqrt{\mu\nu} + t_2 e^{ik} & 0 \end{pmatrix}. \quad (33)$$

$h_b(k) = \vec{B} \cdot \vec{\sigma}$, where the effective magnetic field is

$$\vec{B} = (\sqrt{\mu\nu} + t_2 \cos k, t_2 \sin k, 0). \quad (34)$$

We define a vector field $\mathbf{F}(\mathbf{k}) = (\langle \sigma_x \rangle, \langle \sigma_y \rangle)$ to characterize the topology of $h_b(k)$. The eigenstates associated with $E_{\pm}(k) = \pm \sqrt{(\sqrt{\mu\nu} + t_2 e^{-ik})(\sqrt{\mu\nu} + t_2 e^{ik})}$ are

$$\psi_{\pm}(k) = \frac{1}{\sqrt{2\sqrt{\mu\nu} + 2\sqrt{\mu\nu}t_2 \cos k + t_2^2}} \begin{pmatrix} \pm \sqrt{\sqrt{\mu\nu} + t_2 e^{-ik}} \\ \sqrt{\sqrt{\mu\nu} + t_2 e^{ik}} \end{pmatrix}. \quad (35)$$

The average values of the Pauli matrices associated with the two components effective magnetic field $\langle \sigma_{x,y} \rangle_{\pm} = \langle \psi_{\pm}(k) | \sigma_{x,y} | \psi_{\pm}(k) \rangle$ are

$$\langle \sigma_x \rangle_{\pm} = \frac{\pm(\sqrt{\mu\nu} + t_2 \cos k)}{\sqrt{\mu\nu + 2\sqrt{\mu\nu}t_2 \cos k + t_2^2}}, \quad \langle \sigma_y \rangle_{\pm} = \frac{\pm t_2 \sin k}{\sqrt{\mu\nu + 2\sqrt{\mu\nu}t_2 \cos k + t_2^2}}, \quad (36)$$

i.e., $(\langle\sigma_x\rangle_{\pm}, \langle\sigma_y\rangle_{\pm}) = (B_x, B_y)/E_{\pm}$; thus, $(\langle\sigma_x\rangle_{\pm}, \langle\sigma_y\rangle_{\pm})$ reflects the topological properties of the Bloch bands and the system. The vector field $\mathbf{F}(\mathbf{k})$ under either eigenstate yields the same winding number $w = \oint_L (2\pi)^{-1} (\hat{F}_x \nabla \hat{F}_y - \hat{F}_y \nabla \hat{F}_x) d\mathbf{k}$ in the parameter plane $\mathbf{k} = (k, t_2)$, where $\hat{F}_{x(y)} = F_{x(y)}/\sqrt{F_x^2 + F_y^2}$ and $\nabla = \partial/\partial\mathbf{k}$. The winding number is a topological invariant, characterizing the system topology. The topological phase transition occurs at $(k, t_2) = (0, -\sqrt{\mu\nu})$ or $(\pm\pi, \sqrt{\mu\nu})$, which are the gapless degeneracy points. They are topological defects in the vector field possessing integer topological charges (vortices and antivortices) as depicted in Fig. 3(a).

For $\mu\nu < 0$, the Bloch Hamiltonian reduces to

$$h_b(k) = \begin{pmatrix} 0 & i\sqrt{-\mu\nu} + t_2 e^{-ik} \\ i\sqrt{-\mu\nu} + t_2 e^{ik} & 0 \end{pmatrix}. \quad (37)$$

where the effective magnetic field is

$$\vec{B} = (i\sqrt{-\mu\nu} + t_2 \cos k, t_2 \sin k, 0). \quad (38)$$

the eigenvalues are $E_{\pm}(k) = \pm\sqrt{(i\sqrt{-\mu\nu} + t_2 e^{-ik})(i\sqrt{-\mu\nu} + t_2 e^{ik})}$; correspondingly, the eigenstates are

$$\psi_{\pm}(k) = \frac{1}{\sqrt{\Delta}} \begin{pmatrix} \pm\sqrt{i\sqrt{-\mu\nu} + t_2 e^{-ik}} \\ \sqrt{i\sqrt{-\mu\nu} + t_2 e^{ik}} \end{pmatrix}, \quad (39)$$

where $\Delta = \sqrt{t_2^2 - 2\sqrt{-\mu\nu}t_2 \sin k - \mu\nu} + \sqrt{t_2^2 + 2\sqrt{-\mu\nu}t_2 \sin k - \mu\nu}$.

The average values of $\langle\sigma_{x,y}\rangle_{\pm} = \langle\psi_{\pm}(k)|\sigma_{x,y}|\psi_{\pm}(k)\rangle$ are

$$\langle\sigma_x\rangle_{\pm} = \frac{\pm(\sqrt{e^{-2ik}t_2^2 - \mu\nu} + \sqrt{e^{2ik}t_2^2 - \mu\nu})}{\Delta}, \quad \langle\sigma_y\rangle_{\pm} = \frac{\pm i(\sqrt{e^{-2ik}t_2^2 - \mu\nu} - \sqrt{e^{2ik}t_2^2 - \mu\nu})}{\Delta}. \quad (40)$$

The topological phase transition points are at $(k, t_2) = (\pm\pi/2, \pm\sqrt{-\mu\nu})$, which are the gapless exceptional points. They are topological defects in the vector field possessing half-integer topological charges (vortices and antivortices) as depicted in Fig. 3(b).

Two-dimensional brick wall lattice

The Hamiltonian of the two-dimensional (2D) brick wall lattice is schematically illustrated in Figs. 5(a) and 5(b). In the momentum space, the Bloch Hamiltonians $H_a^{(2D)}(k)$ and $H_b^{(2D)}(k)$ are

$$H_a^{(2D)}(k) = \begin{pmatrix} 0 & 2\mu \cos(k_y) & 0 & t_2 e^{-ik_x} \\ 2\nu \cos(k_y) & 0 & t_2 e^{ik_x} & 0 \\ 0 & t_2 e^{-ik_x} & 0 & 2\mu \cos(k_y) \\ t_2 e^{ik_x} & 0 & 2\nu \cos(k_y) & 0 \end{pmatrix}, \quad (41)$$

$$H_b^{(2D)}(k) = \begin{pmatrix} 0 & 2\mu \cos(k_y) & 0 & t_2 e^{-ik_x} \\ 2\nu \cos(k_y) & 0 & t_2 e^{ik_x} & 0 \\ 0 & t_2 e^{-ik_x} & 0 & 2\nu \cos(k_y) \\ t_2 e^{ik_x} & 0 & 2\mu \cos(k_y) & 0 \end{pmatrix}. \quad (42)$$

The topological phase transition points, and the vortices or antivortices associated with the topological phase transition points in the Brillouin zone in the $k_x - k_y$ space are shown in Figs. 5(c) and 5(d), which are in accords with that revealed in Figs. 3(a) and 3(b).

Under a unitary transformation

$$U_b^{(2D)} = \begin{pmatrix} \sqrt{\nu} & 0 & 0 & 0 \\ 0 & \sqrt{\mu} & 0 & 0 \\ 0 & 0 & \sqrt{\mu} & 0 \\ 0 & 0 & 0 & \sqrt{\nu} \end{pmatrix}, \quad (43)$$

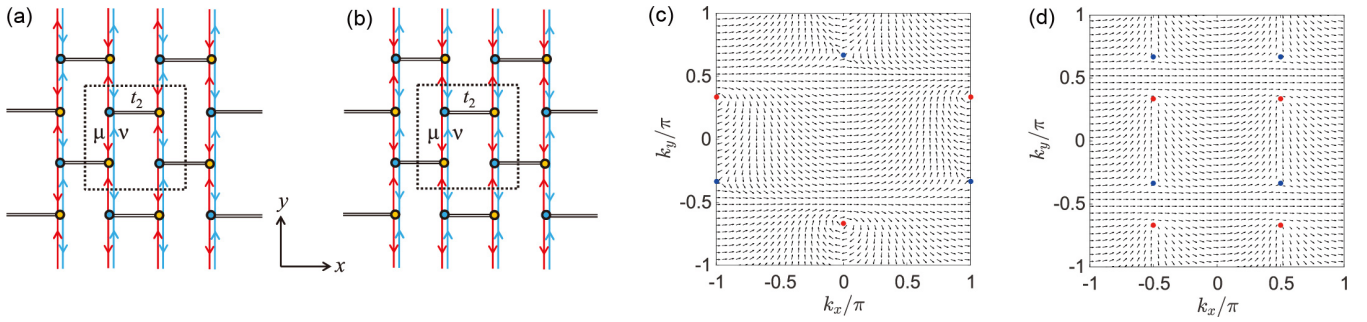


FIG. 5. (a), (b) Schematic of the 2D brick wall lattice. In the x -direction of the 2D lattices are the 1D non-Hermitian SSH lattice in Figs. 1(a) and 1(b), respectively. (c, d) The vector field $\mathbf{F}(k_x, k_y)$ associated with the $E_{b,+}^{(2D)}$ state. (c) $\mu\nu = 1$, (d) $\mu\nu = -1$; and $t_2 = 1$.

the Bloch Hamiltonian $H_b^{(2D)}(k)$ changes into

$$U_b^{(2D)} H_b^{(2D)}(k) U_b^{(2D)-1} = \begin{pmatrix} 0 & 2\sqrt{\mu\nu} \cos k_y & 0 & t_2 e^{-ik_x} \\ 2\sqrt{\mu\nu} \cos k_y & 0 & t_2 e^{ik_x} & 0 \\ 0 & t_2 e^{-ik_x} & 0 & 2\sqrt{\mu\nu} \cos k_y \\ t_2 e^{ik_x} & 0 & 2\sqrt{\mu\nu} \cos k_y & 0 \end{pmatrix}, \quad (44)$$

and the corresponding two-site unit cell Bloch Hamiltonian is

$$h_b^{(2D)} = \begin{pmatrix} 0 & 2\sqrt{\mu\nu} \cos k_y + t_2 e^{-ik_x} \\ 2\sqrt{\mu\nu} \cos k_y + t_2 e^{ik_x} & 0 \end{pmatrix}. \quad (45)$$

the eigenvalues are $E_{b,\pm}^{(2D)} = \pm \sqrt{t_2^2 + 4\sqrt{\mu\nu} \cos k_x \cos k_y + 4\mu\nu \cos^2 k_y}$.

Edge states for systems with defective unit cell at boundary

For system b with an even site number (total site number $N = 4n - 2$), we consider that the Hamiltonian H_b under OBC with two sites [inside the red rectangle in Fig. 1(b)] at the right boundary are missing. Two zero edge states localize at the left and the right boundaries, respectively. The edge state localized at the right boundary is $\psi_{2j-1} = 0$ and

$$\psi_{N-2j} = -[(\nu + \mu) + (-1)^j (\nu - \mu)] / (2t_2) \psi_{N+2-2j}. \quad (46)$$

at large system size limit ($N \gg 1$). For the anomalous edge states at the high order exceptional points ($t_1^2 = \gamma^2$), they are localized at single unit cell at system boundary. For $t_1 = -\gamma$, the left (right) edge state is $\psi_1 = 1$ ($\psi_N = 1$); and for $t_1 = \gamma$, the right edge state is $\psi_N = 1$; the left edge state is $\psi_1 = -(+)\psi_3 = 1$ for $t_1/t_2 > 0$ ($t_1/t_2 < 0$).

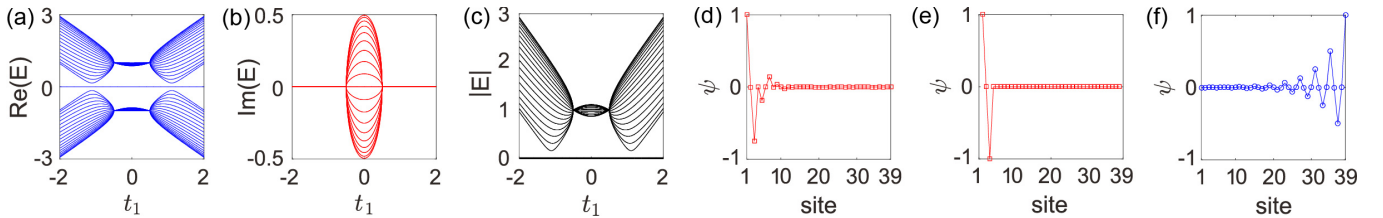


FIG. 6. (a-c) Energy spectra of system b with $N = 39$ at parameters $\gamma = 1/2$ and $t_2 = 1$. The zero edge states at (d) $t_1 = 1/4$, (e) $t_1 = 1/2$, and (f) $t_1 = 3/2$.

For system b with an odd site number, the energy spectra are depicted in Figs. 6(a)–6(c). Only one zero edge state exists in this situation. Considering that the unit cell at the right boundary is defective. In the situation that

$|\mu\nu| < t_2^2$, the edge state localizes at the left boundary, the wave function is Eq. (8); in the situation that $|\mu\nu| > t_2^2$, for the system with site number $N = 4n - 1$, the edge state localized at the right boundary is $\psi_{2j} = 0$ and

$$\psi_{N-2j} = -(2t_2) / [(\mu + \nu) + (-1)^j (\mu - \nu)] \psi_{N+2-2j}; \quad (47)$$

for the system with site number $N = 4n - 3$, the edge state localized at the right boundary is $\psi_{2j} = 0$ and

$$\psi_{N-2j} = -(2t_2) / [(\nu + \mu) + (-1)^j (\nu - \mu)] \psi_{N+2-2j}. \quad (48)$$

For the anomalous edge states at the high order exceptional points ($t_1^2 = \gamma^2$) and the systems with site numbers $N = 4n - 1$ and $4n - 3$, the left edge state is $\psi_1 = - (+) \psi_3 = 1$ for $t_1/t_2 > 0$ ($t_1/t_2 < 0$) at $t_1 = \gamma$ and $\psi_1 = 1$ at $t_1 = -\gamma$.

In contrast, for system *a* with an odd site number has a defective unit cell at the right boundary, only one zero state exists. The right boundary state is $\psi_{2j} = 0$ and $\psi_{N-2j} = (-t_2/\nu) \psi_{N+2-2j}$ when $|t_2| < \sqrt{\mu\nu}$ [83, 92, 93]. At the high order exceptional points, the zero state localizes at one site on the left boundary $\psi_1 = 1$ for $t_1 = -\gamma$; and the zero state is extended, being $\psi_{2j} = 0$ and $\psi_{2j-1} = - (+) \psi_{2j+1}$ for $t_1 = \gamma$ at $t_1/t_2 > 0$ ($t_1/t_2 < 0$).

Energy spectra for complex asymmetric coupling

For system *b* at $\gamma = \sqrt{1/2}e^{i\pi/4}$, the topological phase transition points are at $t_1 = \pm \sqrt[4]{3/4} \approx 0.93$ and $|\cos(k)| = \sqrt{(2 + \sqrt{3})/2}$. The gapless degeneracy points may not be seen in the discrete system with small system size due to the finite number of discrete k . The energy spectra for $\gamma = \sqrt{1/2}e^{i\pi/4}$ are depicted in Fig. 7 for $N = 40$. The nonvanishing gap in $|E|$ shown inside the green circles in Fig. 7(a) is a finite size effect of the discrete system; as N increases, the gap vanishes and gapless degeneracy points reveal.

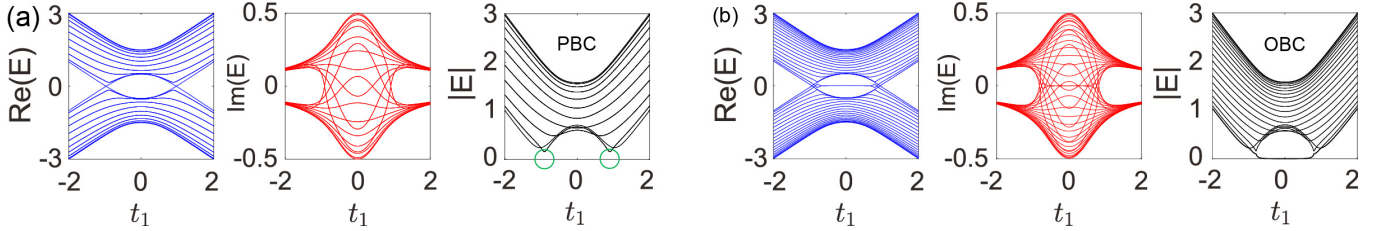


FIG. 7. Energy spectra of system *b* under (a) PBC and (b) OBC for $N = 40$. The parameters are $\gamma = \sqrt{1/2}e^{i\pi/4}$, and $t_2 = 1$.

Chiral-inversion symmetric systems

System *b'* is system *b* with the asymmetric couplings (ν, μ) in the red unit cell [Fig. 1(b)] with an additional minus sign in front [(ν, μ) substituted by $(-\nu, -\mu)$], the Bloch Hamiltonian of system *b'* reads

$$H_{b'}(k) = \begin{pmatrix} 0 & \mu & 0 & t_2 e^{ik} \\ \nu & 0 & t_2 & 0 \\ 0 & t_2 & 0 & -\nu \\ t_2 e^{-ik} & 0 & -\mu & 0 \end{pmatrix}. \quad (49)$$

For even n , systems *b* and *b'* in the real-space are connected through a unitary transformation

$$U_{b'b} = P_{n/2} \otimes \sigma_y \otimes \begin{pmatrix} 0 & 0 & 0 & 1 \\ 0 & 0 & -1 & 0 \\ 0 & -1 & 0 & 0 \\ -1 & 0 & 0 & 0 \end{pmatrix}, \quad (50)$$

that

$$U_{b'b} H_{b'} U_{b'b}^{-1} = H_b. \quad (51)$$

Therefore, systems b and b' have identical band structures and topological properties.

The Bloch Hamiltonian satisfies

$$(\mathcal{SP}) H_{b'}(k) (\mathcal{SP})^{-1} = -H_{b'}(-k) \quad (52)$$

where $\mathcal{SP} = \sigma_y \otimes \sigma_x$. For the Hamiltonian in the real-space, we have

$$U_{\mathcal{SP}} H_{b'} U_{\mathcal{SP}}^{-1} = -H_{b'} \quad (53)$$

where $U_{\mathcal{SP}} = P_n \otimes (\sigma_y \otimes \sigma_x)$. System b' has the combined chiral-inversion symmetry; the chiral symmetry is satisfied that $\mathcal{S} H_{b'} \mathcal{S}^{-1} = -H_{b'}$ with $\mathcal{S} = I_{2n} \otimes \sigma_z$, but the inversion symmetry is violated.

System b with alternative on-site gain and loss $\{i\Gamma, -i\Gamma, i\Gamma, -i\Gamma\}$ introduced in the four-site unit cell possesses the chiral-inversion symmetry, the Bloch Hamiltonian satisfies

$$(\mathcal{SP}) H_b(k) (\mathcal{SP})^{-1} = -H_b(-k) \quad (54)$$

where $\mathcal{SP} = \sigma_x \otimes \sigma_y$. For the Hamiltonian in the momentum space, we have

$$U_{\mathcal{SP}} H_b U_{\mathcal{SP}}^{-1} = -H_b \quad (55)$$

where $U_{\mathcal{SP}} = P_{2n} \otimes \sigma_y$. Notably, both the chiral symmetry and the inversion symmetry are violated. The energy spectra under PBC and OBC are depicted in Figs. 8(a) and 8(b), respectively.

In contrast, the system with on-site term introduced in the four-site unit cell of system b in the form of $\{i\Gamma, -i\Gamma, -i\Gamma, i\Gamma\}$ has the inversion symmetry without chiral symmetry; however, the chiral-inversion symmetry holds. In this case, Eqs. (54) and (55) are satisfied under corresponding operations.

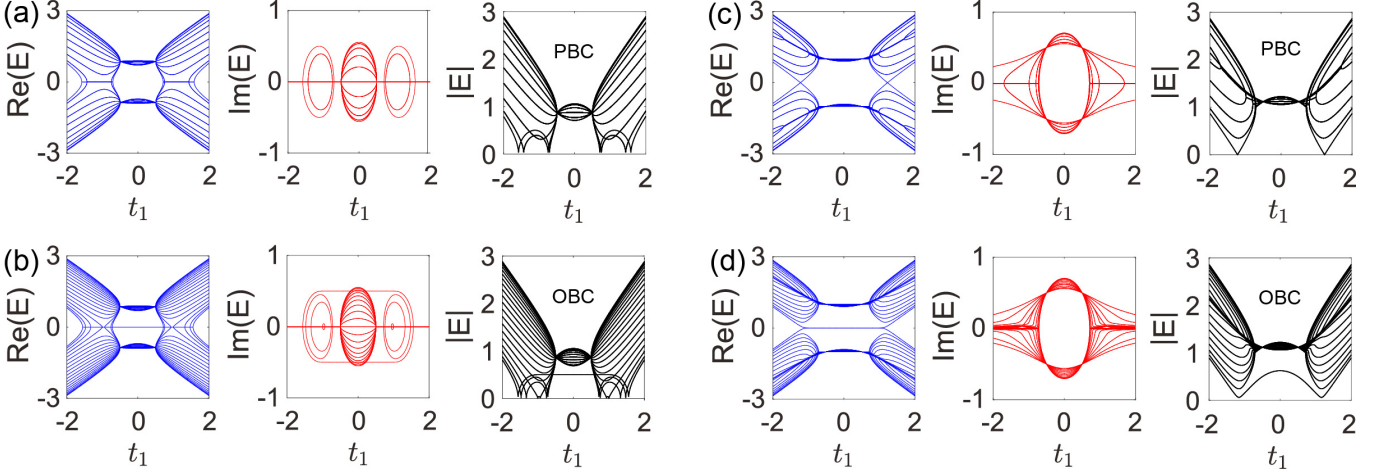


FIG. 8. Energy spectra for systems with staggered gain and loss Γ under PBC and OBC for chiral-inversion symmetric systems (a, b) without chiral symmetry and inversion symmetry $\{i\Gamma, -i\Gamma, i\Gamma, -i\Gamma\}$, and (c, d) without chiral symmetry but with inversion symmetry $\{i\Gamma, -i\Gamma, -i\Gamma, i\Gamma\}$. The parameters are $N = 40$, $\gamma = 1/2$, $\Gamma = 1/2$, and $t_2 = 1$.

The operator \mathcal{SP} is for the Bloch Hamiltonian

$$\mathcal{SP} = \begin{pmatrix} 0 & \mu & 0 & 0 \\ -\nu & 0 & 0 & 0 \\ 0 & 0 & 0 & \nu e^{-ik} \\ 0 & 0 & -\mu e^{-ik} & 0 \end{pmatrix}, \quad (56)$$

and the elements in the unitary transformation $U_{\mathcal{SP}}$ for the Hamiltonian in the real-space are

$$U_{\mathcal{SP}}(i, j) = M_{\mu\nu}(i, j + 2), \quad (57)$$

where $j = j + N$ and

$$M_{\mu\nu} = P_n \otimes \begin{pmatrix} 0 & 0 & 0 & \mu \\ 0 & 0 & -\nu & 0 \\ 0 & \nu & 0 & 0 \\ -\mu & 0 & 0 & 0 \end{pmatrix}. \quad (58)$$

Their energy spectra under PBC and OBC are in Figs. 8(c) and 8(d). System a with $\{i\Gamma, -i\Gamma\}$ introduced in the unit cell has identical (different) spectrum under OBC (PBC) with that of system b composed by introducing $\{i\Gamma, -i\Gamma, i\Gamma, -i\Gamma\}$ aiming to fix the chiral-inversion symmetry in system a . Notably, the gapless degeneracy (exceptional) points in the energy spectra of the systems under PBC and OBC are in accords with each other; the system boundary does not alter most of the bulk states, and the bulk states are all extended states.

Notably, we would like to point out that if we chosen $k = \pi m/n$, $m \in [1, 2n]$ instead of $k = 2\pi m/n$, $m \in [1, n]$, this does not influence the energy bands. The Bloch Hamiltonian of the inversion symmetric system with $\{i\Gamma, -i\Gamma, -i\Gamma, i\Gamma\}$ in its unit cell is rewritten as

$$\begin{pmatrix} i\Gamma & \mu & 0 & t_2 e^{-ik} \\ \nu & -i\Gamma & t_2 e^{ik} & 0 \\ 0 & t_2 e^{-ik} & -i\Gamma & \nu \\ t_2 e^{ik} & 0 & \mu & i\Gamma \end{pmatrix}. \quad (59)$$

Correspondingly, the unitary transformation of \mathcal{SP} is k independent

$$\mathcal{SP} = \begin{pmatrix} 0 & \mu & 0 & 0 \\ -\nu & 0 & 0 & 0 \\ 0 & 0 & 0 & \nu \\ 0 & 0 & -\mu & 0 \end{pmatrix}. \quad (60)$$

-
- * jinliang@nankai.edu.cn
- [1] A. Y. Kitaev, Unpaired Majorana fermions in quantum wires, *Phys. Usp.* **44**, 131 (2001).
 - [2] S. Ryu and Y. Hatsugai, Topological Origin of Zero-Energy Edge States in Particle-Hole Symmetric Systems, *Phys. Rev. Lett.* **89**, 077002 (2002).
 - [3] M. Greiner, O. Mandel, T. Esslinger, T. W. Hänsch, and I. Bloch, Quantum phase transition from a superfluid to a Mott insulator in a gas of ultracold atoms. *Nature* **415**, 39 (2002).
 - [4] S. Murakami, N. Nagaosa, and S. C. Zhang, Spin-hall insulator, *Phys. Rev. Lett.* **93**, 156804 (2004).
 - [5] C. L. Kane and E. J. Mele, Quantum Spin Hall Effect in Graphene, *Phys. Rev. Lett.* **95**, 226801 (2005).
 - [6] B. A. Bernevig, T. L. Hughes, and S. C. Zhang, Quantum spin Hall effect and topological phase transition in HgTe quantum wells, *Science* **314**, 1757 (2006).
 - [7] L. Fu and C. L. Kane, Topological insulators with inversion symmetry, *Phys. Rev. B* **76**, 045302 (2007).
 - [8] L. Fu, C. Kane, and E. Mele, Topological Insulators in Three Dimensions, *Phys. Rev. Lett.* **98**, 106803 (2007).
 - [9] A. P. Schnyder, S. Ryu, A. Furusaki, and A. W. W. Ludwig, Classification of topological insulators and superconductors in three spatial dimensions, *Phys. Rev. B* **78**, 195125 (2008).
 - [10] S. Ryu, A. P. Schnyder, A. Furusaki, and A. W. W. Ludwig, Topological insulators and superconductors: tenfold way and dimensional hierarchy, *New J. Phys.* **12** 065010 (2010).
 - [11] M. Z. Hasan and C. L. Kane, Colloquium: Topological insulators, *Rev. Mod. Phys.* **82**, 3045 (2010).
 - [12] G. Xu, H. Weng, Z. Wang, X. Dai, and Z. Fang, Chern Semimetal and the Quantized Anomalous Hall Effect in HgCr₂Se₄, *Phys. Rev. Lett.* **107**, 186806 (2011).
 - [13] A. A. Burkov and L. Balents, Weyl semimetal in a topological insulator multilayer, *Phys. Rev. Lett.* **107**, 127205 (2011).
 - [14] X.-L. Qi and S.-C. Zhang, Topological insulators and superconductors, *Rev. Mod. Phys.* **83**, 1057 (2011).
 - [15] S. M. Young, S. Zaheer, J. C. Y. Teo, C. L. Kane, E. J. Mele, and A. M. Rappe, Dirac Semimetal in Three Dimensions, *Phys. Rev. Lett.* **108**, 140405 (2012).
 - [16] Z. Wang, Y. Sun, X.-Q. Chen, C. Franchini, G. Xu, H. Weng, X. Dai, and Z. Fang, Dirac semimetal and topological phase transitions in A₃Bi (A=Na, K, Rb), *Phys. Rev. B* **85**, 195320 (2012).
 - [17] C.-E. Bardyn, M. A. Baranov, E. Rico, A. İmamoğlu, P. Zoller, and S. Diehl, Majorana modes in driven-dissipative atomic superfluids with a zero Chern number, *Phys. Rev. Lett.* **109**, 130402 (2012).
 - [18] L. Tarruell, D. Greif, T. Uehlinger, G. Jotzu, and T. Esslinger, Creating, moving and merging Dirac points with a Fermi gas in a tunable honeycomb lattice, *Nature* **483**, 302 (2012).
 - [19] Z. Wang, H. Weng, Q. Wu, X. Dai, and Z. Fang, Three-dimensional Dirac semimetal and quantum transport in Cd₃As₂, *Phys. Rev. B* **88**, 125427 (2013).
 - [20] Z. K. Liu, B. Zhou, Y. Zhang, Z. J. Wang, H. M. Weng, D. Prabhakaran, S.-K. Mo, Z. X. Shen, Z. Fang, X.

- Dai, Z. Hussain, and Y. L. Chen, Discovery of a Three-Dimensional Topological Dirac Semimetal, Na_3Bi , *Science* **343**, 864 (2014).
- [21] M. Xiao, G. Ma, Z. Yang, P. Sheng, Z. Q. Zhang, and C. T. Chan, Geometric phase and band inversion in periodic acoustic systems, *Nat. Phys.* **11**, 240 (2015).
- [22] H. Weng, C. Fang, Z. Fang, B. A. Bernevig, and X. Dai, Weyl Semimetal Phase in Noncentrosymmetric Transition-Metal Monophosphides, *Phys. Rev. X* **5**, 011029 (2015).
- [23] L. Lu, Z. Wang, D. Ye, L. Ran, L. Fu, J. D. Joannopoulos, and M. Soljačić, Experimental observation of Weyl points, *Science*, **349**, 622 (2015).
- [24] D. Leykam, M. C. Rechtsman, and Y. D. Chong, Anomalous Topological Phases and Unpaired Dirac Cones in Photonic Floquet Topological Insulators, *Phys. Rev. Lett.* **117**, 013902 (2016).
- [25] C.-K. Chiu, J. C. Y. Teo, A. P. Schnyder, and S. Ryu, Classification of topological quantum matter with symmetries, *Rev. Mod. Phys.* **88**, 035005 (2016).
- [26] F. K. Kunst, G. van Miert, and E. J. Bergholtz, Lattice models with exactly solvable topological hinge and corner states, *Phys. Rev. B* **97**, 241405 (2018).
- [27] N. P. Armitage, E. J. Mele, and A. Vishwanath, Weyl and Dirac semimetals in three-dimensional solids, *Rev. Mod. Phys.* **90**, 015001 (2018).
- [28] C. M. Bender, Making sense of non-Hermitian Hamiltonians, *Rep. Prog. Phys.* **70**, 947 (2007).
- [29] K. G. Makris, R. El-Ganainy, D. N. Christodoulides, and Z. H. Musslimani, Beam Dynamics in PT Symmetric Optical Lattices, *Phys. Rev. Lett.* **100**, 103904 (2008).
- [30] I. Rotter, A non-Hermitian Hamilton operator and the physics of open quantum systems, *J. Phys. A* **42**, 153001 (2009).
- [31] Z. H. Musslimani, K. G. Makris, R. El-Ganainy, and D. N. Christodoulides, Optical Solitons in PT Periodic Potentials, *Phys. Rev. Lett.* **100**, 030402 (2008).
- [32] A. Guo, G. J. Salamo, D. Duchesne, R. Morandotti, M. Volatier-Ravat, V. Aimez, G. A. Siviloglou, and D. N. Christodoulides, PT-Symmetry Breaking and Laser-Absorber Modes in Optical Scattering Systems, *Phys. Rev. Lett.* **103**, 093902 (2009).
- [33] C. E. Rüter, K. G. Makris, R. El-Ganainy, D. N. Christodoulides, M. Segev, and D. Kip, Observation of parity-time symmetry in optics, *Nat. Phys.* **6**, 192 (2010).
- [34] N. Moiseyev, *Non-Hermitian Quantum Mechanics* (Cambridge Univ. Press, 2011).
- [35] A. Regensburger, M.-A. Miri, C. Bersch, J. Näger, G. Onishchukov, D. N. Christodoulides, and Ulf Peschel, Observation of Defect States in PT-Symmetric Optical Lattices, *PRL* **110**, 223902 (2013).
- [36] B. Peng, S. K. Ozdemir, F. Lei, F. Monifi, M. Gianfreda, G. L. Long, S. Fan, F. Nori, C. M. Bender, and L. Yang, Parity-time-symmetric whispering-gallery microcavities, *Nat. Phys.* **10**, 394 (2014).
- [37] L. Chang, X. Jiang, S. Hua, C. Yang, J. Wen, L. Jiang, G. Li, G. Wang, and M. Xiao, Parity-time symmetry and variable optical isolation in active-passive-coupled microresonators, *Nat. Photon.* **8**, 524 (2014).
- [38] H. Cao and J. Wiersig, Dielectric microcavities: Model systems for wave chaos and non-Hermitian physics, *Rev. Mod. Phys.* **87**, 61 (2015).
- [39] K. Ding, G. Ma, M. Xiao, Z. Q. Zhang, and C. T. Chan, Emergence, Coalescence, and Topological Properties of Multiple Exceptional Points and Their Experimental Realization, *Phys. Rev. X* **6**, 021007 (2016).
- [40] A. Cerjan, A. Raman, and S. Fan, Exceptional Contours and Band Structure Design in Parity-Time Symmetric Photonic Crystals, *Phys. Rev. Lett.* **116**, 203902 (2016).
- [41] Z. Zhang, Y. Zhang, J. Sheng, L. Yang, M.-A. Miri, D. N. Christodoulides, B. He, Y. Zhang, and M. Xiao, Observation of Parity-Time Symmetry in Optically Induced Atomic Lattices, *Phys. Rev. Lett.* **117**, 123601 (2016).
- [42] W. Chen, S. K. Ozdemir, G. Zhao, J. Wiersig, and L. Yang, Exceptional points enhance sensing in an optical microcavity, *Nature* **548**, 192 (2017).
- [43] H. Hodaie, A. U. Hassan, S. Wittek, H. Garcia-Gracia, R. El-Ganainy, D. N. Christodoulides, and M. Khajavikhan, *Nature* **548**, 187 (2017).
- [44] K. Kawabata, Y. Ashida, and M. Ueda, Information Retrieval and Criticality in Parity-Time-Symmetric Systems, *Phys. Rev. Lett.* **119**, 190401 (2017).
- [45] Y. Ashida, S. Furukawa, and M. Ueda, Parity-time-symmetric quantum critical phenomena, *Nat. Commun.* **8**, 15791 (2017).
- [46] H. Zhou, C. Peng, Y. Yoon, C. W. Hsu, K. A. Nelson, L. Fu, J. D. Joannopoulos, M. Soljačić, and B. Zhen, Observation of bulk Fermi arc and polarization half charge from paired exceptional points, *Science* **359**, 1009 (2018).
- [47] R. El-Ganainy, K. G. Makris, M. Khajavikhan, Z. H. Musslimani, S. Rotter, and D. N. Christodoulides, *Nat. Phys.* **14**, 11 (2018).
- [48] W. D. Heiss and H. L. Harney, The chirality of exceptional points, *Eur. Phys. J. D* **17**, 149 (2001).
- [49] C. Dembowski, H.-D. Gräf, H. L. Harney, A. Heine, W. D. Heiss, H. Rehfeld, and A. Richter, Experimental Observation of the Topological Structure of Exceptional Points, *Phys. Rev. Lett.* **86**, 787 (2001).
- [50] M. V. Berry, *Czech. J. Phys.* **54**, 1039 (2004).
- [51] A. A. Mailybaev, O. N. Kirillov, and A. P. Seyranian, Geometric phase around exceptional points, *Phys. Rev. A* **72**, 014104 (2005).
- [52] M. Müller and I. Rotter, Exceptional points in open quantum systems, *J. Phys. A: Math. Theor.* **41**, 244018 (2008).
- [53] R. Uzdin, A. Mailybaev, and N. Moiseyev, On the observability and asymmetry of adiabatic state flips generated by exceptional points, *J. Phys. A* **44**, 435302 (2011).
- [54] W. D. Heiss, The physics of exceptional points, *J. Phys. A* **45**, 444016 (2012).
- [55] S.-D. Liang and G.-Y. Huang, Topological invariance and global Berry phase in non-Hermitian systems, *Phys. Rev. A* **87**, 012118 (2013).
- [56] B. Zhen, C. W. Hsu, Y. Igarashi, L. Lu, I. Kaminer, A. Pick, S.-L. Chua, J. D. Joannopoulos, and M. Soljačić, *Nature* **525**, 354 (2015).
- [57] J. Doppler, A. A. Mailybaev, J. Böhm, U. Kuhl, A. Girschik, F. Libisch, T. J. Milburn, P. Rabl, N. Moiseyev, and S. Rotter, Dynamically encircling an exceptional point for asymmetric mode switching, *Nature* **537**, 76 (2016).
- [58] H. Xu, D. Mason, L. Jiang, and J. G. E. Harris, Topological energy transfer in an optomechanical system with

- exceptional points, *Nature* **537**, 80 (2016).
- [59] D. Heiss, Circling exceptional points, *Nat. Phys.* **12**, 823 (2016).
- [60] A. U. Hassan, B. Zhen, M. Soljačić, M. Khajavikhan, and D. N. Christodoulides, *Phys. Rev. Lett.* **118**, 093002 (2017).
- [61] T. Goldzak, A. A. Mailybaev, and Nimrod Moiseyev, Light Stops at Exceptional Points, *Phys. Rev. Lett.* **120**, 013901 (2018).
- [62] X.-L. Zhang, S. Wang, B. Hou, and C. T. Chan, Dynamically Encircling Exceptional Points: In situ Control of Encircling Loops and the Role of the Starting Point *Phys. Rev. X* **8**, 021066 (2018).
- [63] K. Ding, G. Ma, Z. Q. Zhang, and C. T. Chan, Experimental Demonstration of an Anisotropic Exceptional Point, *Phys. Rev. Lett.* **121**, 085702 (2018)
- [64] L. Jin and Z. Song, Incident Direction Independent Wave Propagation and Unidirectional Lasing, *Phys. Rev. Lett.* **121**, 073901 (2018)
- [65] M. Hafezi, E. A. Demler, M. D. Lukin, and J. M. Taylor, Robust optical delay lines with topological protection, *Nat. Phys.* **7**, 907 (2011).
- [66] M. Aidelsburger, M. Atala, M. Lohse, J. T. Barreiro, B. Paredes, and I. Bloch, Realization of the Hofstadter Hamiltonian with Ultracold Atoms in Optical Lattices, *Phys. Rev. Lett.* **111**, 185301 (2013).
- [67] M. Atala, M. Aidelsburger, J. T. Barreiro, D. Abanin, Takuya Kitagawa, E. Demler, and I. Bloch, Direct measurement of the Zak phase in topological Bloch bands, *Nature Phys.* **9**, 795 (2013)
- [68] L. Lu, J. D. Joannopoulos, and M. Soljačić, Topological photonics, *Nat. Photon.* **8**, 821 (2014).
- [69] S. Mittal, S. Ganeshan, J. Fan, A. Vaez, and M. Hafezi, Measurement of topological invariants in a 2D photonic system, *Nat. Photon.* **10**, 180 (2016).
- [70] Q. Lin, M. Xiao, L. Yuan, and S. Fan, Photonic Weyl point in a two-dimensional resonator lattice with a synthetic frequency dimension, *Nat. Commun.* **7**, 13731 (2016).
- [71] N. Goldman, J. C. Budich, and P. Zoller, Topological quantum matter with ultracold gases in optical lattices, *Nat. Phys.* **12**, 639 (2016).
- [72] S. Diehl, E. Rico, M. A. Baranov, and P. Zoller, Topology by dissipation in atomic quantum wires, *Nat. Phys.* **7**, 971 (2011).
- [73] Y. C. Hu and T. L. Hughes, Absence of topological insulator phases in non-Hermitian PT-symmetric Hamiltonians, *Phys. Rev. B* **84**, 153101 (2011).
- [74] K. Esaki, M. Sato, K. Hasebe, and M. Kohmoto, Edge states and topological phases in non-Hermitian systems, *Phys. Rev. B* **84**, 205128 (2011).
- [75] G. Q. Liang and Y. D. Chong, Optical Resonator Analog of a Two-Dimensional Topological Insulator, *Phys. Rev. Lett.* **110**, 203904 (2013).
- [76] H. Schomerus, Topologically protected midgap states in complex photonic lattices, *Opt. Lett.* **38**, 1912 (2013).
- [77] B. Zhu, R. Lü, and S. Chen, PT symmetry in the non-Hermitian Su-Schrieffer-Heeger model with complex boundary potentials, *Phys. Rev. A* **89**, 062102 (2014).
- [78] J. M. Zeuner, M. C. Rechtsman, Y. Plotnik, Y. Lumer, S. Nolte, M. S. Rudner, M. Segev, and A. Szameit, Observation of a Topological Transition in the Bulk of a Non-Hermitian System, *Phys. Rev. Lett.* **115**, 040402 (2015).
- [79] C. Yuce, Topological phase in a non-Hermitian PT-symmetric system, *Phys. Lett. A* **379**, 1213 (2015).
- [80] X. Wang, T. Liu, Y. Xiong, and P. Tong, Spontaneous PT-symmetry breaking in non-Hermitian Kitaev and extended Kitaev models, *Phys. Rev. A* **92**, 012116 (2015).
- [81] C. Poli, M. Bellec, U. Kuhl, F. Mortessagne, and H. Schomerus, Selective enhancement of topologically induced interface states in a dielectric resonator chain, *Nat. Commun.* **6**, 6710 (2015).
- [82] S. Malzard, C. Poli, and H. Schomerus, Topologically Protected Defect States in Open Photonic Systems with Non-Hermitian Charge-Conjugation and Parity-Time Symmetry, *Phys. Rev. Lett.* **115**, 200402 (2015).
- [83] T. E. Lee, Anomalous Edge State in a Non-Hermitian Lattice, *Phys. Rev. Lett.* **116**, 133903 (2016).
- [84] S. Weimann, M. Kremer, Y. Plotnik, Y. Lumer, S. Nolte, K. G. Makris, M. Segev, M. C. Rechtsman, and A. Szameit, Topologically protected bound states in photonic parity-time-symmetric crystals, *Nat. Mater.* **16**, 433 (2017).
- [85] L. Xiao, X. Zhan, Z. H. Bian, K. K. Wang, X. Zhang, X. P. Wang, J. Li, K. Mochizuki, D. Kim, N. Kawakami, W. Yi, H. Obuse, B. C. Sanders, and P. Xue, Observation of topological edge states in parity-time-symmetric quantum walks, *Nat. Phys.* **13**, 1117 (2017).
- [86] L. Jin, P. Wang, and Z. Song, Su-Schrieffer-Heeger chain with one pair of PT-symmetric defects, *Sci. Rep.* **7**, 5903 (2017).
- [87] M. Klett, H. Cartarius, D. Dast, J. Main, and G. Wunner, Relation between PT-symmetry breaking and topologically nontrivial phases in the Su-Schrieffer-Heeger and Kitaev models, *Phys. Rev. A* **95**, 053626 (2017).
- [88] L. Jin, Topological phases and edge states in a non-Hermitian trimerized optical lattice, *Phys. Rev. A* **96**, 032103 (2017).
- [89] D. Leykam, K. Y. Bliokh, C. Huang, Y. D. Chong, and F. Nori, Edge Modes, Degeneracies, and Topological Numbers in Non-Hermitian Systems, *Phys. Rev. Lett.* **118**, 040401 (2017).
- [90] Y. Xu, S.-T. Wang, and L.-M. Duan, Weyl Exceptional Rings in a Three-Dimensional Dissipative Cold Atomic Gas, *Phys. Rev. Lett.* **118**, 045701 (2017).
- [91] H. Shen, B. Zhen, and L. Fu, Topological Band Theory for Non-Hermitian Hamiltonians, *Phys. Rev. Lett.* **120**, 146402 (2018).
- [92] F. K. Kunst, E. Edvardsson, J. C. Budich, and E. J. Bergholtz, Biorthogonal Bulk-Boundary Correspondence in Non-Hermitian Systems, *Phys. Rev. Lett.* **121**, 026808 (2018).
- [93] S. Yao and Z. Wang, Edge States and Topological Invariants of Non-Hermitian Systems, *Phys. Rev. Lett.* **121**, 086803 (2018).
- [94] V. M. Martinez Alvarez, J. E. Barrios Vargas, and L. E. F. Foa Torres, Non-Hermitian robust edge states in one dimension: Anomalous localization and eigenspace condensation at exceptional points, *Phys. Rev. B* **97**, 121401(R) (2018).
- [95] A. Y. Song, P. B. Catrysse, and S. Fan, Broadband Control of Topological Nodes in Electromagnetic Fields, *Phys. Rev. Lett.* **120**, 193903 (2018).
- [96] S. Lieu, Topological phases in the non-Hermitian Su-Schrieffer-Heeger model, *Phys. Rev. B* **97**, 045106 (2018).

- (2018).
- [97] C. Yin, H. Jiang, L. Li, R. Lü, and S. Chen, Geometrical meaning of winding number and its characterization of topological phases in one-dimensional chiral non-Hermitian systems, *Phys. Rev. A* **97**, 052115 (2018).
- [98] Y. Xiong, Why does bulk boundary correspondence fail in some non-hermitian topological models, *J. Phys. Commun.* **2**, 035043 (2018).
- [99] Z. Gong, Y. Ashida, K. Kawabata, K. Takasan, S. Higashikawa, and M. Ueda, Topological phases of non-Hermitian systems, arXiv:1802.07964.
- [100] K. Kawabata, Y. Ashida, H. Katsura, and M. Ueda, Parity-time-symmetric topological superconductor, *Phys. Rev. B* **98**, 085116 (2018).
- [101] H. Shen and L. Fu, Quantum Oscillation from In-Gap States and a Non-Hermitian Landau Level Problem, *Phys. Rev. Lett.* **121**, 026403 (2018).
- [102] R. Wang, X. Z. Zhang, and Z. Song, Dynamical topological invariant for non-Hermitian Rice-Mele model, arXiv:1804.09975 (accepted by *Phys. Rev. A*).
- [103] M. Klett, H. Cartarius, D. Dast, J. Main, and G. Wunner, Topological edge states in the Su-Schrieffer-Heeger model subject to balanced particle gain and loss, arXiv:1802.06128.
- [104] S. Yao, F. Song, and Z. Wang, Non-Hermitian Chern bands, arXiv:1804.04672.
- [105] K. Kawabata, S. Higashikawa, Z. Gong, Y. Ashida, and M. Ueda, Topological unification of time-reversal and particle-hole symmetries in non-Hermitian physics, arXiv:1804.04676.
- [106] S. Malzard and H. Schomerus, Bulk and edge-state arcs in non-hermitian coupled-resonator arrays, arXiv:1805.08161.
- [107] L. J. Lang, Y. Wang, H. Wang, and Y. D. Chong, Effects of Non-Hermiticity on Su-Schrieffer-Heeger Defect States, arXiv:1807.07776.
- [108] S. Lieu, Topological symmetry classes for non-Hermitian models and connections to the bosonic Bogoliubov-de Gennes equation, arXiv:1807.03320
- [109] H. Jiang, C. Yang, and S. Chen, Topological invariants, phase diagrams and discrepancy for non-Hermitian systems without chiral symmetry, arXiv:1809.00850.
- [110] W. P. Su, J. R. Schrieffer, and A. J. Heeger, Solitons in polyacetylene, *Phys. Rev. Lett.* **42**, 1698 (1979).
- [111] Ref. [102] provides a case of an asymmetric intercell coupling (t_2), where the chiral-inversion symmetry holds and the bulk-boundary correspondence is applicable as discussed in this Letter.
- [112] See online Supplemental Material for more details on the connections between systems, the system symmetries, the topological characterization, the edge states, and additional energy spectra for chiral-inversion symmetric system without chiral and chiral symmetries.
- [113] S. Lin, L. Jin, and Z. Song, Topological quantum phase transition in a non-Hermitian system, arXiv:1712.03814 (2017).
- [114] K. Sun, W. V. Liu, A. Hemmerich, and S. Das Sarma, Topological semimetal in a fermionic optical lattice, *Nat. Phys.* **8**, 67 (2012).
- [115] J. M. Hou, Hidden-Symmetry-Protected Topological Semimetals on a Square Lattice, *Phys. Rev. Lett.* **111**, 130403 (2013).
- [116] Eq. 7 indicates the boundary $t_1 = 0$ for $\gamma = t_2$, which is in accord with that stated in Ref. [93]: zero states should span in region $[-1/\sqrt{2}, 1/\sqrt{2}]$ in Fig. 3 of Ref. [83]. The two disconnected lines occurs in Ref. [83] is a finite size effect, and will vanish at $N \rightarrow \infty$.
- [117] S. Lin and Z. Song, Wide-range-tunable Dirac-cone band structure in a chiral-time-symmetric non-Hermitian system, *Phys. Rev. A* **96**, 052121 (2017).
- [118] L. Ge, Symmetry-protected zero-mode laser with a tunable spatial profile, *Phys. Rev. A* **95**, 023812 (2017).
- [119] B. Qi, L. Zhang, and L. Ge, Defect States Emerging from a Non-Hermitian Flatband of Photonic Zero Modes, *Phys. Rev. Lett.* **120**, 093901 (2018).
- [120] If the asymmetric intracell coupling $\mu\nu$ at boundary vanishes instead of the intercell coupling t_2 , the conclusion for the existence of zero edge states is inverse as in the regions $t_1^2 < \gamma^2 - t_2^2$ and $t_1^2 > \gamma^2 + t_2^2$.
- [121] N. Hatano and D. R. Nelson, Localization Transitions in Non-Hermitian Quantum Mechanics, *Phys. Rev. Lett.* **77**, 570 (1996).
- [122] S. Longhi, D. Gatti, and G. Della Valle, Non-Hermitian transparency and one-way transport in low-dimensional lattices by an imaginary gauge field, *Phys. Rev. B* **92**, 094204 (2015).
- [123] C. Li, L. Jin, and Z. Song, Non-Hermitian interferometer: Unidirectional amplification without distortion, *Phys. Rev. A* **95**, 022125 (2017).